Published in final edited form as:
J Geophys Res. 2009 March ; 114(E3): . doi:10.1029/2008JE003285.

Thermal Tides in the Martian Middle Atmosphere as Seen by the Mars Climate Sounder

C. Lee[1], **W. G. Lawson**[1], **M. I. Richardson**[1], **N. G. Heavens**[1], **A. Kleinböhl**[2], **D. Banfield**[3], **D. J. McCleese**[2], **R. Zurek**[2], **D. Kass**[2], **J. T. Schofield**[2], **C. B. Leovy**[4], **F. W. Taylor**[5], and **A. D. Toigo**[3]

[1]Division of Geological and Planetary Sciences, California Institute of Technology

[2]Jet Propulsion Laboratory, California Institute of Technology

[3]Department of Astronomy, Cornell University

[4]Department of Atmospheric Sciences, University of Washington

[5]Department of Physics, University of Oxford

Abstract

The first systematic observations of the middle atmosphere of Mars (35km–80km) with the Mars Climate Sounder (MCS) show dramatic patterns of diurnal thermal variation, evident in retrievals of temperature and water ice opacity. At the time of writing, the dataset of MCS limb retrievals is sufficient for spectral analysis within a limited range of latitudes and seasons. This analysis shows that these thermal variations are almost exclusively associated with a diurnal thermal tide. Using a Martian General Circulation Model to extend our analysis we show that the diurnal thermal tide dominates these patterns for all latitudes and all seasons.

1. Introduction

The diurnal solar forcing of the thin Martian atmosphere drives large-amplitude planetary-scale oscillations known as atmospheric thermal tides [Gierasch and Goody, 1968; Zurek, 1976; Leovy , 1981]. These tides have been seen in lander records of daily varying surface pressure and near–surface winds [Hess et al. , 1977; Leovy , 1981; Tillman, 1988; Murphy et al., 1996; Schofield et al., 1997], especially during periods of high dust opacity [Leovy and Zurek, 1979]. Away from the surface tides have been revealed through spectral analysis of Viking and Mars Global Surveyor (MGS) air temperature data [Banfield et al., 2000, 2003; Martin, 1981, though also see Wilson and Richardson [2000]] and of very high altitude density variations in data taken during spacecraft aerobraking [Forbes et al., 2002; Wilson, 2002].

Thermal tides are the harmonic response of the atmosphere to time–varying insolation, through either direct absorption of sunlight or through heating of the surface and subsequent

C. Lee, Division of Geological and Planetary Sciences, California Institute of Technology M/C 150-21 Pasadena, CA 91125, USA (lee@gps.caltech.edu).

heat exchange with the atmosphere. Since solar forcing is not a simple sinusoid, its excited modes, too, span a range of wavenumbers and frequencies. In the Mars atmosphere these daily oscillations are a significant fraction of the total natural variability. Furthermore, some components of these tides have the character of vertically propagating internal gravity waves, whose amplitude will grow exponentially as density decreases with altitude and thereby provide a potent driver of middle and upper atmosphere flows. One effect of their interaction with the background circulation is to amplify downwelling that adiabatically warms the high-latitude regions. Observationally these vertically propagating tidal components should produce large-amplitude temperature oscillations with height that change phase throughout the day. To capture these waves requires observation with scale–height to half–scale–height vertical resolution, particularly in the middle martian atmosphere (35–80km) where the tidal temperature oscillations are large [e.g. Zurek, 1978; Wilson and Hamilton, 1996].

While observations from the Thermal Emission Spectrometer (TES) onboard MGS are able to observe the middle atmosphere when in limb–view mode, these observations have not been described in any detail in the published literature. Recently, however, systematic observations from the Mars Reconnaissance Orbiter (MRO) Mars Climate Sounder (MCS) have become available that map the Martian atmosphere from near the surface to roughly 80 km with near 5 km vertical resolution [McCleese et al., 2007]. These new temperature and aerosol opacity retrievals from MCS limb radiance observations provide a regular and sustained look into tidal activity within the middle atmosphere [McCleese et al., 2008]. What the MCS observations reveal is a pattern in the middle Mars atmosphere day-night temperature contrasts that is remarkably consistent with the lowest-order solar synchronous diurnal tidal mode expected from classical tidal theory [Zurek, 1976]. The observed presence of this pattern provides a powerful test of more sophisticated model simulations and these models in turn can help characterize the full range of tidal behavior that cannot be observed directly due to orbital constraints of the satellite and incomplete coverage of the retrieved fields. Successful simulation of the observed tides in the middle atmosphere is a key step in validation of models of the general circulation of the Mars atmosphere and in aiding our understanding of atmospheric transport of water vapor and aerosol.

A basic description of classical tidal theory and some of its extensions in nonlinear numerical models are given in Section 2. Section 3 describes the data analysis we applied to the MCS retrievals: this includes both basic longitudinal (zonal) averaging and more detailed Fourier analysis. Only so much can be done given the coverage in the current set of retrievals, thus in Section 4 we introduce the MarsWRF GCM, a tool we use to extend the analysis of tides in the middle atmosphere. In section 5 we compare in detail the results from WRF and MCS for the L_s 135°–165° period, and we discuss the latitude–height structures present in the retrieved water ice clouds. Section 6 contains the results of the GCM analysis — first we make a plausibility argument that the GCM is a valid simulation of the data *for the purposes of analyzing the tides*, then we proceed with the extended analysis capitalizing on having complete spatial and local time coverage. Finally, we recapitulate our conclusions in Section 7.

2. Review of Theory and Models

Dynamically, thermal tides are a mixture of vertically trapped and vertically propagating internal gravity waves whose periods are determined by daily varying solar forcing. There is no appreciable gravitational tide in the atmosphere from either the Sun or Mars's two small moons [Rondanelli et al., 2006]. For the ideal case of a solar forcing of a stationary atmosphere on a sphere with no topographic variation, the excited linear wave modes are described by the product of functions of local time, latitude, and altitude. The latitude functions are called Hough modes, which are the eigenfunctions of Laplace's tidal equation, each with an associated eigenvalue proportional to an equivalent depth, by analogy with the tidal modes of a global ocean of a single depth. Whether or not the vertical structure functions grow in amplitude with altitude depends on the ratio of the atmospheric scale height to this equivalent depth, modulated by the static stability. Modes dominated by rotation have negative equivalent depths and are vertically trapped. Modes with positive, moderately large equivalent depths propagate vertically and are efficiently excited, whether for Earth or Mars [Chapman and Lindzen, 1970]. Thus, in the classical theory, the dominant mode for daily temperature variations in the middle atmosphere is the lowest order solar synchronous diurnal Hough mode. Such a mode follows the sun's apparent westward motion with a fixed phase lag which varies with height but not time. Furthermore, this mode has two distinct characteristics [Zurek, 1976]. First, it has a vertical wavelength of

$$L \sim \frac{2\pi H}{\sqrt{\frac{SH}{h} - \frac{1}{4}}}, \quad (1)$$

where H, h, and S are the scale height, equivalent depth and a static stability parameter. For typical parameters L ≈30 km (see Fig. 1 for a typical profile). Second, this mode has a phase reversal with latitude at $\theta \approx 22°$, with largest amplitudes close to the equator.

This classical view is an approximation from the linearized primitive equations of momentum, mass continuity, energy equation, and ideal gas law. In an atmosphere that is not isothermal, not at rest, and (importantly for Mars) one above topographic variations which are large comparable to an atmospheric scale height, other factors come into play. The topographic variations can modify the tidal oscillations both by modifying the solar heating (e.g., thinner air over high regions has a larger response to surface heating) and by coupling the dynamical response to large topographic features (e.g., flow is diverted around topographic obstacles). These factors modify the tide in several ways: wavelengths can be stretched spatially by the background structure in wind and temperature and modes are excited which are not simple functions of local time. Stated differently in the latter case, tides are generated which do not appear fixed with respect to the sun's apparent motion.

Previous perturbations to tidal theory suggest that the most important of these topographically induced tides is the diurnal Kelvin mode, an eastward propagating diurnally varying mode which has a vertical structure close to the natural atmospheric resonance [Zurek, 1976, 1988; Hamilton and Garcia , 1986]. This mode has (in the semi-classical theory) a cosine-like structure in latitude with no phase reversal and with an amplitude that

is fairly constant with height, but possibly large due to the natural resonance of the cold Mars atmosphere. Longitudinal variations in atmospheric opacity can also produce solar asynchronous tidal modes, and the diurnal Kelvin mode can be quite large on Mars during the onset of major dust storms [Zurek and Leovy, 1981].

While the classical theory provides a guide to the nature of the tides in the middle atmosphere, the complications cited above can only be addressed in more complicated models. In fact, tides were prominent in the first GCM simulations of the Mars atmosphere [Leovy and Mintz , 1969], although that two-level model could not properly simulate the vertical structure of the tides. Hamilton [1982] noted that tidal forcing of the zonally symmetric circulation could be large and Zurek [1988] used tidal fluxes computed with a classical tidal model to drive a 6–layer zonally symmetric model, which showed the potential for atmospheric tides to modify the general atmospheric circulation. Current numerical models have the needed vertical resolution to simulate tides more realistically and can show how the background thermal structure and winds can modify the tide, as well as how the tidal response modifies the general flow. This interaction varies with the seasonally changing solar forcing, particularly as the dust loading and direct solar heating of the atmosphere vary with season [e.g. Wilson and Hamilton, 1996]. So, these more general circulation models can be tested with the new observations but also can be used to help separate the various tidal components that cannot be separated observationally due to the incomplete coverage in space and time (see next section).

3. Current observations by MCS

The Mars Climate Sounder (MCS) onboard the Mars Reconnaissance Orbiter (MRO) has been observing the Martian atmosphere since late September 2006 (L_s 111°). MCS is a filter radiometer observing in 8 IR channels and 1 broadband visible channel [McCleese et al., 2007]. MCS observes primarily in a fore-limb geometry (i.e. looking ahead at the horizon of the planet) with approximately a half scale height (5 km) vertical resolution when its fields of view are projected on the limb. Three of the IR channels are located on the wing of the 15 micron CO_2 absorption band. Exploiting both the geometry of the fields-of-view and the differing sensitivities of the three channels allows retrieval of temperature, aerosol opacity, and pressure as functions of height between the surface and roughly 80 km.

The MCS retrieval [McCleese et al., 2008] is based on an iterative scheme following Chahine [1972]. Profiles of dust and water ice opacities are retrieved simultaneously with pressure and temperature, using channels centered on the dust absorption feature at 22 μm and on the water ice absorption maximum at 12μm, respectively. Gases are represented in the radiative transfer with a Curtis–Godson approximation that uses precalculated transmissions for each channel. Both dust and ice are treated as absorbers described by extinction efficiencies derived from Mie calculations spectrally integrated for each channel. The size distribution for the water ice particles was assumed to be a modified gamma distribution with an effective radius of 1.36 μm and an effective variance of 0.14.

Refractive indices for water ice were taken from Warren [1984]. Water ice opacities are given in the unit km^{-1} for a frequency of 843 cm^{-1}, corresponding to the center frequency of

the channel in which they are retrieved. Delivery of MCS retrievals are being made to the PDS atmospheres node.

Since the beginning of mapping, approximately three quarters of a million retrievals have been obtained from the MCS limb radiance observations. The retrievals converge consistently in low to moderate aerosol conditions. Comparison where possible with MGS–TES and radio occultation where appropriate are encouraging, and the results presented in this paper strongly suggest the retrievals do an excellent job of picking up real temperature structures in the middle atmosphere. Conditions with high aerosol opacities, e.g. during dust storms or within the tropical cloud belt, are more difficult to retrieve. In the current dataset retrievals tend to be sparse particularly during daytime in equatorial regions due to high water ice opacities in the tropical cloud belt [Smith et al., 2003].

Figure 1 shows a number of typical profiles taken from the MCS dataset, at approximately 3am or 3pm local–times within a small latitude band (45°–50° north) and L_s band (156°–162°); for comparison, we also show output for similar local–times and latitudes from a Martian General Circulation Model [Richardson et al., 2007], discussed in section 4. The model profiles are similar to the data in some important ways. For example the vertical wavelength appears roughly in agreement, as do the vertical levels of relative minimum and maximum temperatures. Differences occur in terms of the precise amplitude and vertical phase of the tide, and this may result from errors in the prescription of aerosols in the model or modest errors in the background wind structure, for example. At the top of the model, the influence of damping layers appears to accentuate the model day-night temperature differences. Overall, however, the model compares rather well with observations and it should be noted that the simulation was not tuned to match the observations (indeed the model was run prior to the acquisition of the MCS data).

The MCS temperature profiles have all been obtained at roughly 3am or 3pm local time (except at high latitudes) because of the nearly polar, sun-synchronous orbit of the MRO spacecraft. This observation pattern provides excellent spatial resolution and coverage of the entire planet, while maintaining the local time of the observations over seasonal periods. The resulting dataset is best suited to studies of seasonal phenomena and provides a bimodal distribution of local time coverage that places some limitations on the observable spectrum of wave activity in the atmosphere. In particular, the fixed local time of the observations imparts a sampling frequency that is the Nyquist frequency of diurnal waves — this causes aliasing of higher harmonic wave modes [Salby , 1982a, b]. In this study, we augment analysis of the observations by utilizing a numerical model to unscramble the various contributions of the tidal modes to the day-night temperature variations observed by MCS.

MCS has been making almost continuous retrievals of the atmospheric temperature since the start of the mission in late September 2006 (L_s 111°), with the exception of a period during southern spring (L_s 190° – L_s 250°). To date, the majority of the temperature retrievals available are from relatively ‘clear air’ conditions, where the opacity due to aerosols (clouds, hazes and dust) is small to modest. In this work, we concentrate on the start of the Martian year, from L_s 0° through L_s 150° (using data from L_s 345° to L_s 165°), where we have the most complete coverage at all latitudes and times.

As almost all of the MCS observations are made near 3am or 3pm local time, we choose to bin the data centered on these times, with a two hour window extending from 2am to 4am and 2pm to 4pm, respectively. As a result, we lose much of the retrievals poleward of 80° (and 50% of the retrievals poleward of 75° latitude) because these latitudes are not observed at the local times within the specified windows. In order to make the dataset more tractable to analysis, we trade-off time resolution for improved spatial coverage by binning the retrievals into 64 longitude bins, (5.625° width) 36 latitude bins (5° width), and 30° L_s bins, centered on 0°, 30°, 60°, etc. The horizontal resolution is chosen for ease of comparison with a numerical model (see next section), and we retain the vertical resolution of the retrievals as published on the MCS PDS node. The limb viewing geometry produces some notable characteristics of the retrieved profiles; each profile is the average of about 200km of atmosphere along the line of sight of the instrument; adjacent profiles overlap by as much as 50% in their coverage because of the spacing between consecutive observations (they are not completely independent observations). When binning the data, we use the profile latitude and longitude provided by the level 2 data set.

Following Banfield et al. [2000, 2003] (see also Lieberman [1991]) we note that the binned MCS retrievals can be recombined into an "average temperature" (T_{avg}) and a "difference temperature" (T_{diff}), where

$$T_{avg}(\lambda, \theta, p, L_s) = \frac{T(3pm) + T(3am)}{2}, \quad (2)$$

$$T_{diff}(\lambda, \theta, p, L_s) = \frac{T(3pm) - T(3am)}{2}, \quad (3)$$

and λ is longitude, μ is latitude, p is pressure, and L_s is heliocentric longitude. T_{avg} and T_{diff} are the main focus of the analysis that follows. We first examine the longitudinal averages of T_{avg} (equation 2) and T_{diff} (equation 3), and then we examine the spectral decomposition of the same fields.

3.1. Longitudinal Averaging

Figures 2 and 3 show the time and longitudinal average of T_{avg} and T_{diff} for the MCS data. Each subplot in these figures represents a 'month' (30° of L_s) of data, starting at northern vernal equinox (L_s 0°). Latitudes which do not have both a 3am and 3pm retrieval in the current dataset are plotted white (typically in the equatorial region, where aerosol abundance is highest). The left column of figures 2 and 3 shows the northern vernal equinox (top) and northern summer solstice (bottom) 'months'.

Figure 2 shows similar mean temperature features to those observed by other orbiters [e.g. Conrath, 1975; Smith et al., 2001], and the observations are qualitatively similar to GCM predictions for the mean thermal structure of the middle atmosphere [Forget et al., 1999; Haberle et al., 1999; Wilson and Hamilton, 1996; Richardson et al., 2007]. In the solstice

month (L_s 90°) the summer hemisphere surface is warmest with a significant temperature maximum in the middle atmosphere (near 1Pa) connected by an isthmus to the lower atmosphere. During the equinoxes, the equatorial region is warmest with the same middle atmosphere temperature maxima, though weaker, extending into both polar regions. The warming near the surface is due to rapid response of the atmosphere to the radiative forcing [Gierasch and Goody, 1968], while the middle atmosphere temperature maxima are thought to be related to the downwelling branch of the meridional overturning extending into the polar night [Conrath, 1975]. The first MCS observations of this polar warming are reported in McCleese et al. [2008]

The longitudinal average of T_{diff}, shown in figure 3, presents a much different — and quite stunning — field, one that no prior orbiters have seen. A clear pattern of positive and negative extrema (antinodes) is visible in figure 3, centered on a positive extremum at 2Pa above the equator (e.g. during L_s 150°). This pattern is very reminiscent of figure 10 of Zurek and Haberle [1988], which shows the heating due to the diurnal tide, calculated from a coupled axisymmetric-tidal model. We will discuss this pattern in more detail in the next section, after decomposing the temperature data to highlight the dominant wave modes in the T_{avg} and T_{diff} fields.

3.2. Spectral Decomposition

To perform the spectral decomposition of the temperature fields, we first decompose the data into time and longitude components,

$$T(\lambda,\phi,p,t)=\sum_{\sigma}\sum_{s}T_{\sigma,s}(\phi,p)\ cos\left(\sigma\left(t+t_0(\phi,p)\right)+s\left(\lambda+\lambda_0(\phi,p)\right)\right), \tag{4}$$

where temperature T is a function of longitude (λ), latitude (ϕ), pressure (p), and time (t). The wave amplitude $T_{\sigma,s}$ is a function of cycle frequency σ, longitudinal wavenumber s, latitude and pressure. Time and longitude are assumed to have units of radians in this equation, so that one solar day has 2π radians, and 0°–360° longitude corresponds to 0–2π radians. t_0 is the phase offset in time and λ_0 the phase offset in longitude, both are functions of latitude and pressure.

We can then replace the time component t in equation 4 with local time $\tilde{t}$ using the transform $\tilde{t}=t+\lambda+\lambda_0$, with $m=s-\sigma$,

$$T(\lambda,\phi,p,t)=\sum_{\sigma}\sum_{s}T_{\sigma,s}(\phi,p)\ cos\left(\sigma\tilde{t}+m\lambda+\sigma t_0(\phi,p)+m\lambda_0(\phi,p)\right). \tag{5}$$

Finally, we define a temperature $T(m)$ as

$$T(m,\phi,p)=\sum_{s}\sum_{\sigma=m-s}T_{\sigma,s}\ cos\left(\sigma\tilde{t}+m\lambda+\sigma t_0(\phi,p)+m\lambda_0(\phi,p)\right), \tag{6}$$

and

$$T(\lambda,\phi,p,t)=\sum_m T(m,\phi,p)\,. \tag{7}$$

For clarity, we omit the latitude and pressure dependence of $T(m, \phi, p)$ in the remainder of this work, denoting the field as $T(m)$. The *local time wavenumber*, m, is then the wavenumber of the wave mode observed at fixed local time (3pm and 3am for MCS). Each component with a particular value of m will have contributions from a series of aliased longitudinal waves (with different σ, s). For example, $T(m = 0)$ will contain all waves where $s = \sigma$: the zonal mean field ($s = \sigma = 0$), the classical diurnal tide ($s = \sigma = 1$), the classical semi–diurnal tide ($\sigma = s = 2$), and higher harmonics of the sun–synchronous diurnal tide.

Observing this field at two local times separated by 12 hours (3am and 3pm for MCS), we can further separate these modes based on the value of σ. The 12 hour time difference between observations introduces a phase change of $\sigma\pi$ radians between the two local times. This phase change introduces a sign dependence in the form of $(-1)^{\sigma}$:

$$T_{\sigma,s}(\phi,p,3pm)=T_{\sigma,s}(\phi,p)\ cos\left(\sigma\tilde{t}_{3pm}+m\lambda+\sigma t_0+m\lambda_0\right), \tag{8}$$

$$\begin{aligned} T_{\sigma,s}(\phi,p,3am) &= T_{\sigma,s}(\phi,p)\ cos\left(\sigma\tilde{t}_{3am}+m\lambda+\sigma t_0+m\lambda_0\right), \\ &= (-1)^{\sigma}T_{3pm,\sigma,s}. \end{aligned} \tag{9}$$

Combining these terms in equations 2 and 3, we see that T_{avg} will have no contributions from *odd* σ waves, but may have non–zero contributions from *even* σ waves, such as the zonal mean 'wave' ($\sigma = s = m = 0$) or the sun–synchronous semi–diurnal tide ($\sigma = s = 2$, $m = 0$). Similarly, T_{diff} will have no contributions from *even* σ waves, but may have non–zero contributions from *odd* σ waves, such as the sun–synchronous diurnal tide ($\sigma = s = 1$, $m = 0$). Waves with $m = 0$ are sun–synchronous, waves with higher values of m propagate in local time, such as a stationary wavenumber 1 ($\sigma = 0$, $s = 1$, $m = 1$) or the eastward propagating wavenumber 1 diurnal Kelvin wave ($\sigma = -1$, $s = 1$, $m = 2$). The most significant waves and their corresponding m, s and σ values are listed in table 1. We also restrict s and m to be positive definite, meaning $m = |s - \sigma|$, and use positive σ for westward propagation.

We can further decompose each wavemode σ, s into a series of Hough modes. In doing so, we can specify the vertical and latitudinal structure of the mode depending on the Hough modes that contribute to each σ, s mode. We do not perform this decomposition for this work. We note that, *a posteriori*, the sun–synchronous diurnal tide is dominated by the latitudinally broadest Hough mode with positive equivalent depth h — this is the $\Theta(1, 1)$ mode in the notation of Chapman and Lindzen [1970]. We expect to observe a temperature field dominated by modes with positive equivalent depths (and hence vertically propagating modes) because evanescent modes are vertically trapped in the lower atmosphere within vertical layers too narrow to resolve accurately in MCS retrievals.

As the magnitude of the zonal mean temperature is much larger than the amplitude of any wave mode in the atmosphere, we do not expect to see significant contributions from the wave modes (except the zonal mean) in T_{avg} (figure 2). However, the same argument cannot be made for the T_{diff} field (figure 3) because it is comprised entirely of wave modes with no contribution from the zonal mean. Prior work leads us to expect the sun–synchronous diurnal tide will dominate the T_{diff} field [Zurek, 1988; Wilson and Hamilton, 1996; Banfield et al., 2003], and we attempt to confirm that with this dataset, especially within the middle atmosphere which has not previously been the subject of systematic observation.

Figure 4 shows the contribution to the T_{avg} field from $T_{avg}(m = 0)$, which includes contributions from the zonal mean temperature and even wavenumber tides. We bin the data into 8 longitudinal bins (from the original 64 bins) before decomposition in order to increase the longitudinal coverage available from the dataset. We then exclude latitudes where there are not enough points to perform this decomposition, coloring those latitudes white in figure 4.

It is again evident from figure 4 that the zonal mean temperature field ($\sigma = s = 0$) describes much of the structure in figure 2 [for example, see Smith et al., 2001; Banfield et al., 2003]. This result demonstrates the expectation mentioned above that the zonal mean dominates the mean T_{avg} field, at least in the regions amenable to spectral analysis.

In figure 5, we plot the contribution to T_{diff} from $T_{diff}(m = 0)$, which includes the sun–synchronous diurnal tide ($\sigma = s = 1$). The pattern in figure 5 is very similar to the observed pattern (shown in figure 3) and suggests that a large fraction of the signal in the T_{diff} field is due to the $m = 0$ component. However, it is impossible with only two local time bins to decompose the $m = 0$ field into its constituent wave modes, making unambiguous attribution to the diurnal (wavenumber 1) mode difficult. In section 6, we will show that within a GCM simulation this pattern is dominated by the sun–synchronous diurnal tide, thus strongly suggesting the same for the data presented here. Use of a GCM in this capacity immediately offers predictions for the regions currently outside the coverage of the dataset — one such prediction is that there should be a strong seasonal cycle for the amplitude of the $m = 0$ component of T_{diff} within the tropics.

Before moving to examination of the GCM output, it is worth comparing the MCS observations with those from TES. Figures 2 and 3 can be compared with the analogous plots from Banfield et al. [2003] (figures 2 and 7, reproduced from the TES data here in figures 6 and 7). We can see similarities between the TES and MCS data in the lower atmosphere (where they overlap) — this is somewhat expected (at least hoped for) given that the two instruments observed with local times differing only by about an hour. The agreement provides a pleasing cross validation of the two instruments and retrieval techniques. Again, an obvious advantage of the MCS dataset is that its limb retrieval coverage extends significantly higher in altitude and vertical resolution than the TES nadir retrieval dataset, showing a more developed structure within the Martian middle atmosphere.

Finally, to show the seasonal evolution of the temperature fields, figure 8 shows the $m = 0$ mode on a single pressure surface, as a function of time and latitude. From inspection of

figure 3, the peak magnitude is located near 2Pa, hence we use this pressure for all subsequent single level plots. Figure 8 shows a reversal in the latitudinal temperature gradient from that which we observe on the surface – at 2 Pa we see temperatures increasing towards the poles. Moreover, the coldest (zonal mean) temperatures occur near the solstice, with cooling leading up to this period, and warming after.

In the $T_{\text{diff}}(m = 0)$ field, throughout the mid–latitudes the morning (3am) temperatures are warmer than afternoon (3pm) temperatures (shown in figure 8 as a negative magnitude). In the $T_{\text{diff}}(m = 0)$ field, a small, asymmetric seasonal trend is present in the magnitude of the m=0 mode; the northern hemisphere magnitude decreases near northern summer solstice, while the southern hemisphere magnitude increases during the same season. In section 6, we show an equivalent plot from a GCM simulation that encapsulates the structure we would expect to see when more MCS retrievals become available. Indeed, the same fields from WRF exhibit many of the features shown in figure 8, such as the seasonal trend of the mid–latitude T_{diff}.

4. The MarsWRF General Circulation Model

We use a Martian atmospheric GCM as a tool to extend the analysis of tides by calculating the T_{avg} and T_{diff} using the simulated atmosphere of the model. The GCM we use is the PlanetWRF GCM [Richardson et al., 2007] in a Mars configuration. The model is a global, planetary adaptation of the National Center for Atmospheric Research (NCAR) Weather Research and Forecasting (WRF) model. In this study, the MarsWRF GCM is configured with 64 longitude grid points, 36 latitude grid points, and 40 vertical levels using a terrain following coordinate. The conversion to global and planetary use is described by Richardson et al. [2007]. For this study, the Martian version of the model is used with a wide-band radiation scheme to model the radiative absorption and emission within the CO_2 15 μm band and absorption and scattering due to dust. We use a prescribed dust distribution similar to the Mars Climate Database MGS distribution [Lewis et al., 1999; Richardson et al., 2007]. The GCM includes a full CO_2 cycle, topography, and surface albedo and thermal properties that are used to drive a subsurface heat diffusion and surface energy balance scheme. The model compares well to other leading Martian GCMs [see, for example, Figure 4 from Johnson et al., 2008].

For comparison with the MCS data, we use output from the tenth year of a standard MarsWRF simulation, again grouping by ‘months’ (30° of L_s) and by local time — The horizontal resolution for the MCS bins was chosen to coincide with a standard Mars GCM resolution. A powerful advantage of the GCM is that it affords essentially complete coverage of the atmosphere. One consequence is that the local times can be more evenly sampled between 2am and 4am (or 2pm and 4pm) than is possible with the orbit of MRO. Figures 9 and 10 show the time and longitudinal average T_{avg} and T_{diff} plots for the MarsWRF simulation, following the formats of figures 2 and 3. However, for the WRF data we include the latter half of the year for completeness, and the subplots in the top half of figures 9 and 10 correspond to the subplots in figures 2 and 3.

Comparing figure 9 with figure 2, it is evident that the GCM captures much of the thermal structure observed by MCS and TES [Banfield et al., 2003]. The GCM reproduces the T_{avg} temperature structure well, including the near surface maxima and the broad latitudinal gradients in the lower atmosphere. It is also able to reproduce the middle atmosphere pattern with middle atmosphere maxima near 1Pa and 60°–75° degrees of latitude [McCleese et al., 2008] connected to the lower atmosphere tropics. Although the polar maxima are smaller in magnitude (i.e. cooler) in the GCM than is observed, their locations and evolution seems well captured by the model. We discuss the comparison between the GCM and retrievals in more detail in section 5 and explain some of the notable differences there.

The GCM T_{diff} (figure 10) is equally encouraging in comparison to that derived from MCS retrievals (figure 3). We see the same pattern of nodes and anti–nodes, with similar wavelengths (both vertical and horizontal), and amplitude. The extrema (anti–nodes) have approximately the observed locations and their evolution seems to be captured — the model has a strong seasonal cycle which is not evident in the current MCS retrievals, which are most abundant during northern summer in the mid–latitudes, thus making quantitative comparison difficult.

There are some notable differences between the structures simulated in the GCM and those found in the MCS retrievals. For example, the upper atmosphere of the GCM (pressures less than 0.05 Pa) is subject to an eddy Rayleigh damping of the wind and temperature fields in order to reduce spurious reflections from the numerical model top, a consequence of this eddy damping is that some waves will dissipate energy here that might otherwise propagate to lower pressures. In this simulation, the thermal tides are being dissipated at the model top and produce a temperature difference which may be larger than is physically realized in the atmosphere at this pressure, but this dissipation aloft does not disrupt the tidal structure and evolution within the atmosphere's interior. Additionally, the atmospheric temperatures close to the planet surface, within the planetary boundary layer (PBL) of the GCM, are sensitive to the particular parameterization chosen for the PBL and surface models [e.g. Richardson et al., 2007; Heavens et al., 2008]. In this simulation the temperature variation near the surface appears larger than the retrievals for this reason.

However, the simulation and retrievals seem remarkably close, particularly when the T_{avg} and T_{diff} fields are considered together, all the more in light of the agreement of the individual profiles shown in figure 1. Certainly, it seems plausible that the model is capturing the critical processes responsible for the observed patterns and their evolution. To examine more closely the agreement of the GCM with the retrievals, for the purposes of analyzing tides, we provide a more detailed discussion of the comparison of the model and data for the L_s 150° period, where we have the most complete coverage in the retrievals.

5. L_s 150 comparison

The most complete month of retrievals from MCS is the period between L_s 135° and L_s 165°, corresponding to a period just after the conjunction in November 2006 through January 2007; there is a sufficient number of retrievals in this period to see the equatorial temperatures, which is often obscured by the equatorial cloud belt in the current set of

retrievals. Figure 11 shows the T_{diff} field during this season calculated from MCS retrieved temperatures and the WRF simulated temperatures (repeated from figures 3 and 10), and also a schematic showing the important features in these plots. The T_{diff} field from the WRF simulation compares well with the same field calculated from the MCS retrieved temperatures, within the bulk of the atmosphere. The T_{mean} field from WRF (figure 9) also compares well with the same field calculated from MCS retrievals (figure 2), but this field is not as important for the analysis of the sun–synchronous diurnal tide and we do not repeat those figures here.

The schematic (figure 11, right) highlights the features in the T_{diff} plots that are due to the odd wavenumber tidal modes. The figure is included to clarify the pattern shown in the WRF and MCS fields, which consists of a ‘grid’ of antinodes (extrema) of alternating sign with a positive antinode above the equatorial surface in the lower atmosphere. Solar heating of the lower atmosphere and surface produces a warmer atmosphere in the daytime than the night, producing this positive antinode, and the vertical wavelength and horizontal structure of the dominant response (which we show later to be the sun–synchronous diurnal tide) then constrains the pattern of antinodes shown in figure 11. In the sub–tropics and mid–latitudes, the horizontal structure (Hough mode solution) has changed sign so we see antinodes with the opposite sign to those above the equator.

Figure 12 shows the retrieved water ice opacity for this period at 3am and 3pm, binned similarly to the temperature data. At both times, the lower atmosphere water ice opacity is highest in the local temperature minima. The persistence of this pattern throughout the day, and its correlation with the temperature field, suggests that the pattern is controlled by same dynamical phenomenon that causes the pattern in the T_{diff} field.

The spatial/temporal correspondence between the diurnal temperature difference and the ice opacity seems physically consistent and presents evidence for how the tides affect the ice. However, the model currently lacks the feedback of water ice radiative effects on air temperatures, which have recently been suggested to be of importance [Wilson et al., 2008]. Fully self–consistent simulations are needed to explore this in the future.

Based on the good agreement between simulation and the retrievals, in both the T_{mean} and T_{diff} fields, we intend to use the model to extend our analysis of the MCS dataset. Although we intend to use the GCM in this way, it is important to note that our analysis does not rely on the model reproducing the atmospheric state precisely. Thus, we have not attempted to modify our model to achieve better agreement — this is better achieved through systematic data assimilation. Also, using on this approach, we make no claims with absolute quantitative precision about the current state of the atmosphere.

6. Results and Predictions from MarsWRF

As we have access to the full atmospheric state from the MarsWRF simulation we can analyze the data in the spectral domain in addition to the time domain. For example, we are able to calculate the contribution of a particular wave mode to T_{avg} or T_{diff} by filtering the particular wavenumber and frequency range we are interested in, and then reconstructing the

temperature field using the filtered data. We can use this information to guide our investigation and interpretation of the T_{avg} and T_{diff} fields observed by MCS, and our conclusions can later be tested once the MCS dataset coverage becomes sufficiently dense.

A representative example of the data processing we use to calculate the amplitude of each wavemode is given in figure 13. The left panel shows a longitude and time map (Hovmöller diagram) of the simulated temperature at 2Pa at 15° south of the equator, from around L_s 150° (after removing time and longitudinal average values for clarity). The Fourier transform of this data produces the figure in the bottom panel of figure 13. This figure has peaks corresponding to the sun–synchronous diurnal tide and its harmonics (along the diagonal line shown), a baroclinic "weather" mode (the low frequency westerly propagating mode) and a series of wavenumber 1 westerly modes, most likely due to interaction between the diurnal tide and the orography. Further discussion of the decomposition of the temperature field in reference to Martian tides can be found in Read and Lewis [2004] (section 5.2.4).

In order to investigate the contributions to the local time wavenumber $m = 0$, we decompose the T_{avg} and T_{diff} fields from the GCM and filter the full output from the GCM for the largest amplitude wave modes that would appear in the $m = 0$ field, following the equations in section 3.2. We can then readily assess which waves are dominant in the $m = 0$ mode. We include analysis of the latter half of the year (L_s 165° through L_s 345°) as a prediction of what might be observed with MCS when additional retrievals from this period become available.

The $m = 0$ local time wavenumber is the most significant mode here, because the contributing wave modes are responsible for much of the pattern shown in figures 2 and 3, but the higher order local time wavenumbers ($m = 1, 2, 3$) are also interesting because they include contributions from stationary tides and traveling waves (e.g. the diurnal Kelvin waves, see table 1). We do not present the higher local time wavenumbers here due to the low number of MCS retrievals in the regions where these modes are most significant, especially during southern summer.

Figure 14 shows the $T_{avg}(m = 0)$ and $T_{diff}(m = 0)$ fields as a function of L_s and latitude on the 2 Pa surface, and also the largest magnitude contributions to these fields, listed in table 1. The left column of this figure can be compared to figure 8 which shows the same decomposition for the first half of the Martian year from the MCS retrievals.

The most significant wave component of $T_{avg}(m = 0)$ is the zonal mean field (with a mean value of about 150K) that explains the vast majority of the $T_{avg}(m = 0)$ field over all pressure levels and seasons. The sun–synchronous semi–diurnal tide explains much less of the signal. Its greatest contribution, though still small, is during southern summer (L_s 270°), consistent with its role as a proxy for dust loading [Zurek and Leovy, 1981; Wilson and Richardson, 2000; Lewis and Barker, 2005]. The $T_{diff}(m = 0)$ field (figure 14, lower left) is dominated by a strong sun-synchronous diurnal component (figure 14, lower center). The ter–diurnal mode (figure 14, lower right) is much weaker and, like the semi–diurnal mode, is most important during southern summer (L_s 270°). The higher wavenumber modes

contribute even less to the $T_{avg}(m = 0)$ and $T_{diff}(m = 0)$ fields and are not plotted here. Note that although we only show one pressure level here, these fields show similar structure over many levels (as does the MCS dataset), however, limited space prevents use from showing all 42 levels used in the GCM and all 105 levels used in the MCS retrievals.

There is a strong seasonal dependence evident in the $T_{diff}(m = 0)$ field, and in the sun–synchronous diurnal tide field. The latitude of the peak amplitude follows a sinusoid in L_s (i.e $\theta_{peak} \sim \sin(L_s)$) with an amplitude of about 25°. It is likely that the structure of the tide in the atmosphere is controlled by the background wind (and its latitudinal gradients), which tends to peak in the winter hemisphere near the edge of the polar night. In the MarsWRF simulation, the peak sun–synchronous diurnal tide amplitude occurs near the sub–solar point in the lower atmosphere, but follows closely the equatorward edge of the winter jet into the middle atmosphere (sloping poleward with height). During the equinox seasons, the jet structures are weaker and hemispherically symmetric, hence the sun–synchronous diurnal tide amplitude peaks over the equator at all altitudes. A similar discussion regarding the effect of the background flow is presented in Wilson and Hamilton [1996].

The MarsWRF simulation shows very little seasonal variation in the T_{diff} field for pressures greater than about 150Pa (the lower atmosphere), consistent with the observed pattern not being so evident in the restricted vertical sampling of the TES data [Banfield et al., 2003]. The negative antinode (near 30 Pa) has the same seasonal trend as the positive antinode at 2Pa, while the surface temperature T_{diff} pattern follows the sub–solar point closely. The pattern of antinodes persists throughout the year, but their magnitudes decrease during the southern summer period (L_s 270°–360°) when the planet is closest to the Sun and also when the dust opacity is greatest [e.g. Martin, 1986; Colburn et al., 1989]. This trend is observed in the WRF simulated data and the TES retrievals (in the lower atmosphere, [Banfield et al., 2003]). However, the global dust storm that occurred during this season of the first year of MCS observations complicates the retrieval process for this period.

As the Mars Climate Database [Lewis et al., 1999] is readily available (at http://www-mars.lmd.jussieu.fr/), it is relatively easy to examine this seasonal behavior of the tide in an independent GCM. The MCD dataset produces the same pattern of antinodes we find in MarsWRF and the MCS observations. For example the peak magnitude of the T_{diff} pattern during northern summer, at about 2Pa, is about 10K as found in WRF. We therefore believe that the simulated seasonal behavior is not unique to WRF.

Aside from the latitudinal drift of the $T_{diff}(m = 0)$ (figure 14, lower left) maxima into the southern hemisphere during southern fall and winter, another interesting feature is the reduction in amplitude during the southern summer. This reduction is easier to understand: during this time Mars is closest to the Sun and is forced more strongly by it, because of the increased insolation and increased dustiness of the atmosphere. This additional forcing increases the amplitudes of the wave modes other than the sun–synchronous diurnal tide (e.g. the transient modes found by Banfield et al. [2004]) that tend to disrupt the diurnal tides propagation by modifying the atmospheric structure, especially in the winter hemisphere.

7. Conclusions

The MCS dataset shows dramatic and sustained day–night temperature differences in the middle atmosphere. Spectral analysis of both the MCS retrievals and representative GCM output supports the hypothesis that this temperature difference is due almost entirely to the sun–synchronous diurnal tide.

For mid–latitudes during northern spring and summer, spectral analysis allows us to show directly from the MCS retrievals that the zonal mean temperature dominates the T_{avg} field (3pm and 3am average), and the sun–synchronous diurnal tide dominates the T_{diff} field (3pm and 3am difference). Output from MarsWRF was found to replicate the MCS (and Mars Climate Database) patterns of T_{avg} and T_{diff} adequately for the purposes of interpreting the diurnal temperature differences and disentangling their contributions from tidal modes.

To the extent that the model simulates the Martian atmosphere well, the sun–synchronous diurnal tide dominates the T_{diff} field at all latitudes,heights and seasons. Further, the model makes several predictions that can be tested when the dataset is more complete. Most notably: the sun–synchronous diurnal tide maximum aloft drifts into the southern hemisphere during southern fall and winter, apparently in association with the development of the winter polar jet; the sun–synchronous diurnal tide undergoes great reduction in amplitude in northern winter; the dominant wavenumber in the winter stationary waves follow the dominant high-latitude zonal topographic wavenumber.

Acknowledgments

The authors acknowledge J. Shirley, C. Backus, T. Pavlicek and E. Sayfi for their contribution to the acquisition and analysis of MCS data, and thank the anonymous reviewers for their useful comments and work in improving this manuscript. This work was funded by the National Aeronautics and Space Administration through the Mars Reconnaissance Orbiter project.

References

Arakawa A, Lamb VR. Computational design of the basic dynamical processes of the UCLA General Circulation Model. Methods in Computational Physics. 1977; 17:173–265.

Banfield D, Conrath BJ, Gierasch PJ, Wilson RJ, Smith MD. Traveling waves in the Martian atmosphere from MGS TES Nadir data. Icarus. 2004; 170(2):365–403.

Banfield D, Conrath BJ, Pearl JC, Smith MD, Christensen P. Thermal tides and stationary waves on Mars as revealed by Mars Global Surveyor thermal emission spectrometer. J. Geophys. Res. 2000; 105(E4):9521–9537.

Banfield D, Conrath BJ, Smith MD, Christensen PR, Wilson RJ. Forced waves in the Martian atmosphere from MGS TES nadir data. Icarus. 2003; 161(2):319–345. doi: 10.1016/S0019-1035(02)00044-1.

Cahoy KL, Hinson DP, Tyler GL. Characterization of a semidiurnal eastward-propagating tide at high northern latitudes with Mars Global Surveyor electron density profiles. Geophys. Res. Lett. 2007; 34(15):L15201. doi: 10.1029/2007GL030449.

Chahine MT. A general relaxation method for inverse solution of the full radiative transfer equation. J. Atmos. Sci. 29:741–747.

Chapman, S.; Lindzen, RS. Atmospheric Tides. D. Reidel Publishing Co.; Dordrecht: 1970. p. 200

Colburn DS, Pollack JB, Haberle RM. Diurnal variations in optical depth at Mars. Icarus. 1989; 79(1): 159–189.

Conrath BJ. Thermal structure of the Martian atmosphere during the dissipation of the dust storm of 1971. Icarus. 1975; 24(1):36–46.

Forbes JM, Bridger AFC, Bougher SW, Hagan ME, Hollingsworth JL, Keating GM, Murphy J. Nonmigrating tides in the thermosphere of Mars. J. Geophys. Res. 2002; 107(E11) doi: 10.1029/2001JE001582.

Forget F, Hourdin F, Fournier R, Hourdin C, Talagrand O, Collins M, Lewis SR, Read PL, Huot J-P. Improved general circulation models of the martian atmosphere from the surface to above 80 km. J. Geophys. Res. 1999; 104(E10):24,155–24,175.

Gierasch P, Goody R. A study of the thermal and dynamical structure of the Martian lower atmosphere. Planet. Space Sci. 1968; 16(5):615–636.

Haberle RM, Joshi MM, Murphy JR, Barnes JR, Schofield JT, Wilson G, Lopez-Valverde M, Hollingsworth JL, Bridger AFC, Schaeffer J. General circulation model simulations of the Mars Pathfinder atmospheric structure investigation/meteorology data. J. Geophys. Res. 1999; 104(E4): 8957–8974.

Hamilton K. The effect of solar tides on the general circulation of the Martian atmosphere. J. Atmos. Sci. 1982; 39:481–485.

Hamilton K, Garcia RR. theory and observations of the short–period normal mode oscillations of the atmosphere. J. Geophys. Res. 1986; 91:11867–11875.

Heavens NG, Richardson MI, Toigo AD. Two aerodynamic roughness maps derived from Mars Orbiter Laser Altimeter (MOLA) data and their effects on boundary layer properties in a Mars general circulation model (GCM). J. Geophys. Res.–Planets. 2008; E2:113:E02014. doi: 10.1029/2007JE002991.

Hess SL, Henry RM, Leovy CB, Ryan JA, Tillman JE. Meteorological results from the surface of Mars: Viking 1 and 2. J. Geophys. Res. 1977; 82:4559–4574.

Hollingsworth JL, Barnes JR. Forced stationary planetary waves in Mars's winter atmosphere. J. Atmos. Sci. 1996; 53(3):428–448.

Johnson SS, Mischna MA, Grove TL, Zuber MT. Sulfur–induced greenhouse warming on early Mars. J. Geophys. Res. 2008; 113(E8):E08005. doi: 10.1029/2007JE002962.

Leovy CB. Observations of martian tides over two annual cycles. J. Atmos. Sci. 1981; 28:30–39.

Leovy CB, Mintz Y. Numerical simulation of the atmospheric circulation and climate of Mars. J. Atmos. Sci. 1969; 26:1167–1190.

Leovy CB, Zurek RW. Thermal tides and Martian dust storms: Direct evidence for coupling. J. Geophys. Res. 1979; 84:2956–2968.

Lewis SR, Barker PR. Atmospheric tides in a Mars general circulation model with data assimilation. Adv. Space Res. 2005; 36(11):2162–2168. doi: 10.1016/j.asr.2005.05.122.

Lewis SR, Collins M, Read PL. A climate database for Mars. J. Geophys. Res. 1999; 104(E10): 24,177–24,194.

Lieberman RS. Nonmigrating diurnal tides in the equatorial middle atmosphere. J. Atmos. Sci. 1991; 48(8):112–1123.

Martin TZ. Mean thermal and albedo behavior of the Mars surface and atmosphere over a Martian year. Icarus. 1981; 45(2):427–446.

Martin TZ. Thermal infrared opacity of the Mars atmosphere. Icarus. 1986; 66(1):2–21.

McCleese DJ, Schofield JT, Taylor FW, Calcutt SB, Foote MC, Kass DM, Leovy CB, Paige DA, Read PL, Zurek RW. Mars Climate Sounder: An investigation of thermal and water vapor structure, dust and condensate distributions in the atmosphere, and energy balance processes of the polar regions. J. Geophys. Res. 2007; 112(E5):E05S06. doi: 10.1029/2006JE002790.

McCleese DJ, Schofield JT, Taylor FW, Abdou WA, Aharonson O, Banfield D, Calcutt SB, Heavens NG, Irwin PGJ, Kass DM, Kleinbhl A, Lawson WG, Leovy CB, Lewis SR, Paige DA, Read PL, Richardson MI, Teanby N, Zurek RW. Intense polar temperature inversion in the middle atmosphere on Mars. Nature Geoscience. 2008 doi: 10.1038/ngeo332.

Murphy JR, Leovy CB, Tillman JE. Observations of Martian surface winds at the Viking Lander 1 site. J. Geophys. Res. 1996; 95:14855–14516.

Read, PL.; Lewis, SR. The Martian climate revisited: Atmosphere and environment of a desert planet. Springer–Verlag Berlin and Heidelberg GmbH & Co. K; Berlin: 2004. p. 326

Richardson MI, Toigo AD, Newman CE. PlanetWRF: A general purpose, local to global numerical model for planetary atmospheric and climate dynamics. J. Geophys. Res. 2007; 112(E9):E09001. doi: 10.1029/2006JE002825.

Rondanelli R, Thaylan V, Lindzen RS, Zuber MT. Atmospheric contribution to the dissipation of the gravitational tide of Phobos on Mars. Geophys. Res. Lett. 2006; 33(15):L15201. doi: 10.1029/2006GL026222.

Salby MR. Sampling theory for asynoptic satellite observations. Part I: Space-time spectra, resolution, and aliasing. J. Atmos. Sci. 1982; 39:2577–2600.

Salby MR. Sampling theory for asynoptic satellite observations. Part II: Fast Fourier synoptic mapping. J. Atmos. Sci. 1982; 39:2601–2614.

Schofield JT, Barnes JR, Crisp D, Haberle RM, Larsen S, Magalhes JA, Murphy JR, Seiff A, Wilson G. The Mars Pathfinder Atmospheric Structure Investigation/Meteorology (ASI/MET) Experiment. Science. 1997; 278(1752):1752–1757. doi: 10.1126/science.278.5344.1752. [PubMed: 9388169]

Smith MD, Pearl JC, Conrath BJ, Christensen PR. Thermal Emission Spectrometer results: Mars atmospheric thermal structure and aerosol distribution. J. Geophys. Res. 2001; 106(E10):23,929–23,945.

Smith MD, Bandfield JL, Christensen PR, Richardson MI. Thermal Emission Imaging System (THEMIS) infrared observations of atmospheric dust and water ice cloud optical depth. J. Geophys. Res. 2003; 108 doi:10.1029/2003JE002115.

Tillman JE. Mars global atmospheric oscillations: Annually synchronized, transient normal mode oscillations and the triggering of global dust storms. J. Geophys. Res. 1988; 93:9433–9451.

Warren SG. Optical constants of ice from the ultraviolet to the microwave. Atmos. Optics. 1984; 23:1206–1225.

Wilson RJ. Evidence for diurnal Kelvin waves in the Martian atmosphere from Mars Global Surveyor TES data. Geophys. Res. Lett. 2000; 27(23):3889–3892.

Wilson RJ. Evidence for nonmigrating thermal tides in the Mars upper atmosphere from the Mars Global Surveyor Accelerometer Experiment. Geophys. Res. Lett. 2002; 29(7) doi: 10.1029/2001GL013975.

Wilson RJ, Hamilton K. Comprehensive model simulations of thermal tides in the Martian atmosphere. J. Atmos. Sci. 1996; 53(9):1290–1326.

Wilson RJ, Lewis SR, Montabone L, Smith MD. Influence of water ice clouds on Martian tropical atmospheric temperatures. Geophys. Res. Lett. 2008; 35:L07202. doi:10.1029/2007GL032405.

Wilson RJ, Richardson MI. The Martian atmosphere during the Viking mission, Infrared measurements of atmospheric temperatures revisited. Icarus. 2000; 145(2):555–579. doi: 10.1006/icar.2000.6378.

Zurek RW. Diurnal tide in the Martian atmosphere. J. Atmos. Sci. 1976; 33(2):321–337.

Zurek RW. Solar heating of the Martian dusty atmosphere. Icarus. 1978; 35(2):196–208.

Zurek RW. Free and forced modes in the Martian atmosphere. J. Geophys. Res. 1988; 93(D8):9452–9462.

Zurek RW, Haberle RM. Zonally symmetric response to atmospheric tidal forcing in the dusty Martian atmosphere. J. Atmos. Sci. 1988; 45(18):2469–2485.

Zurek RW, Leovy CB. Thermal tides in the dusty Martian atmosphere: A verification of theory. Science. 1981; 213(4506):437–439. [PubMed: 17760188]

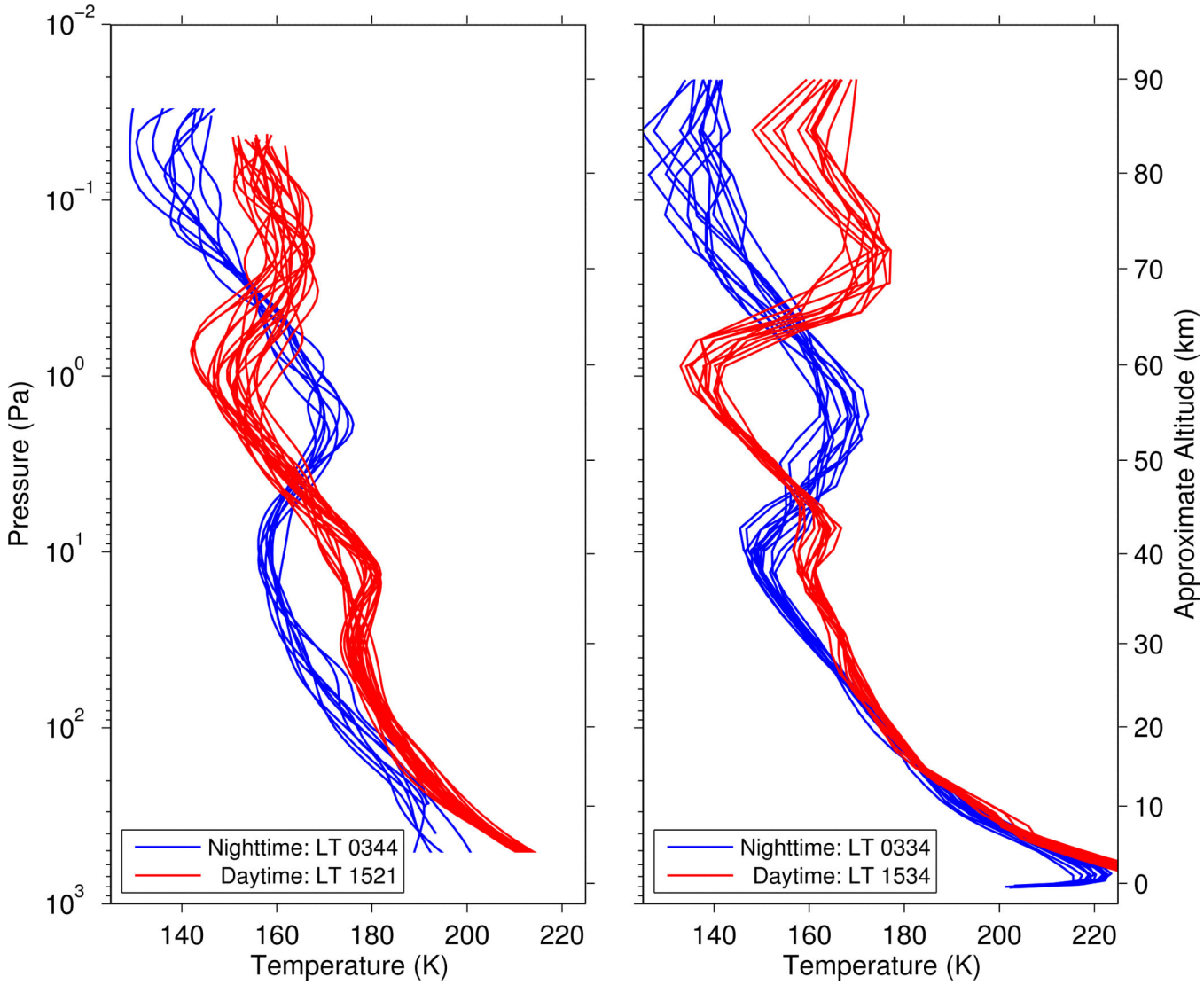

Figure 1.

(left) Selected profiles taken from the MCS dataset between 45° and 50° north, L_s 156°–162° for nighttime (blue) and daytime (red). (right) Selected profiles taken from the WRF output at 47.5° north, L_s 156°–162° for nighttime (blue) and daytime (red).

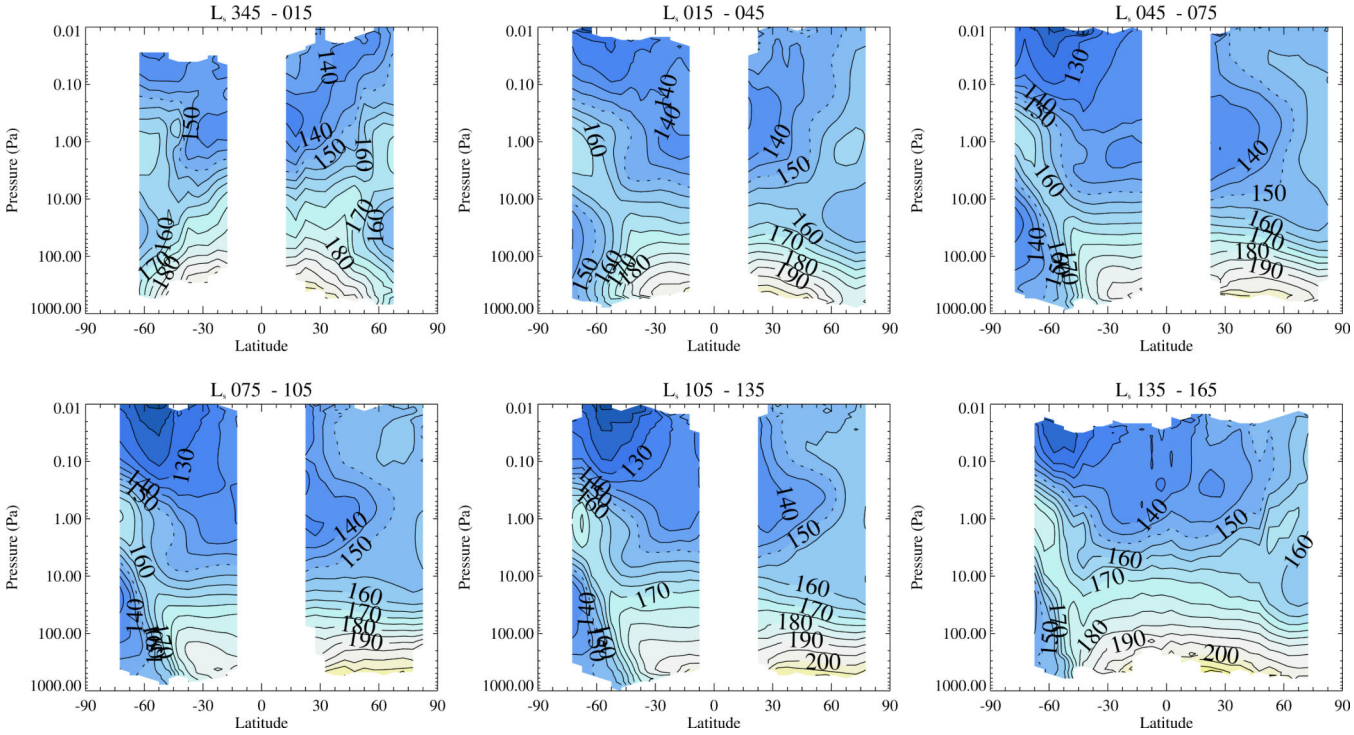

Figure 2.

Longitudinal mean of T_{avg} plotted from MCS retrievals. Data is first binned into 64 longitude bins and 36 latitude bins, using the same vertical layers as the retrievals (105 layers), and binned here into 30° of L_S centered on 0°,30°,60°,90° etc. Latitudes with no retrievals are plotted as blank white. Contour interval is 5K. The dashed temperature contour is 150K (provided for reference).

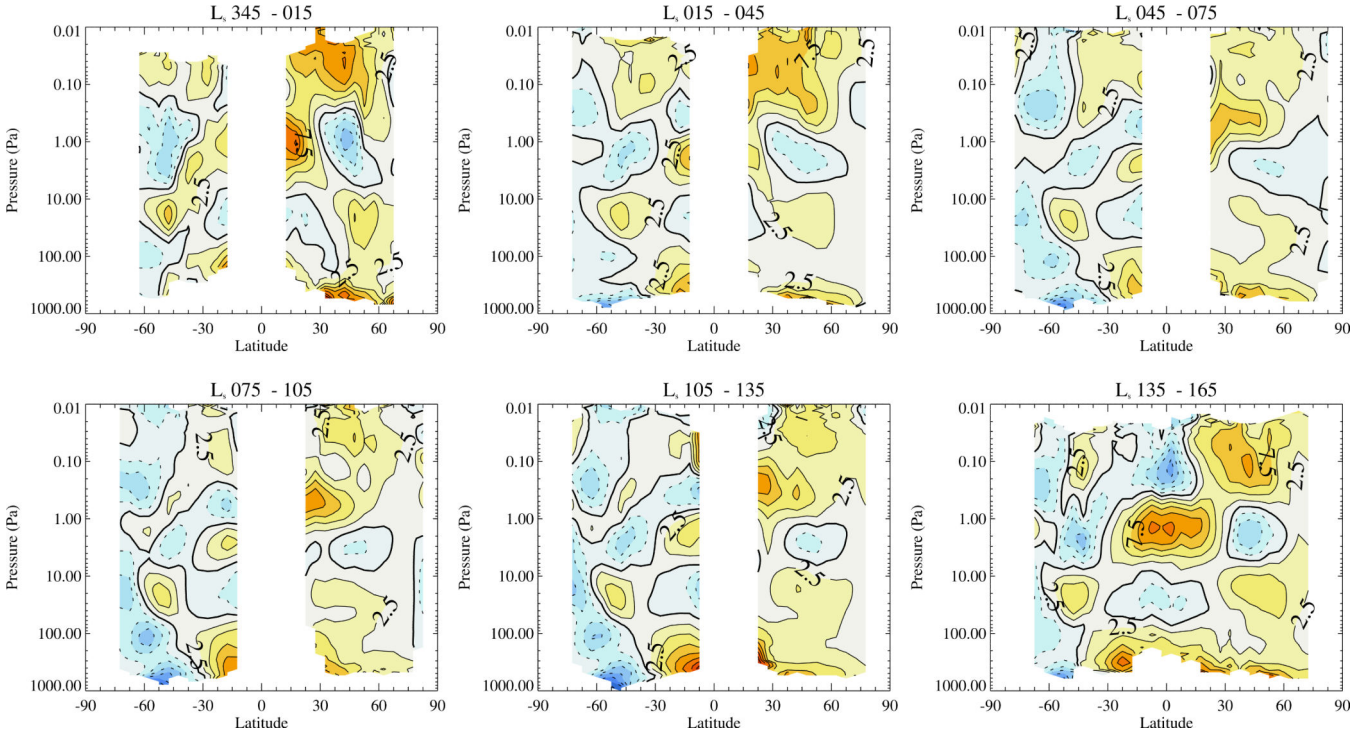

Figure 3.

As figure 2, but T_{diff} from equation 3. Calculated from MCS retrievals. The contour interval is 2.5K and the thick temperature contour is 0K (for reference).

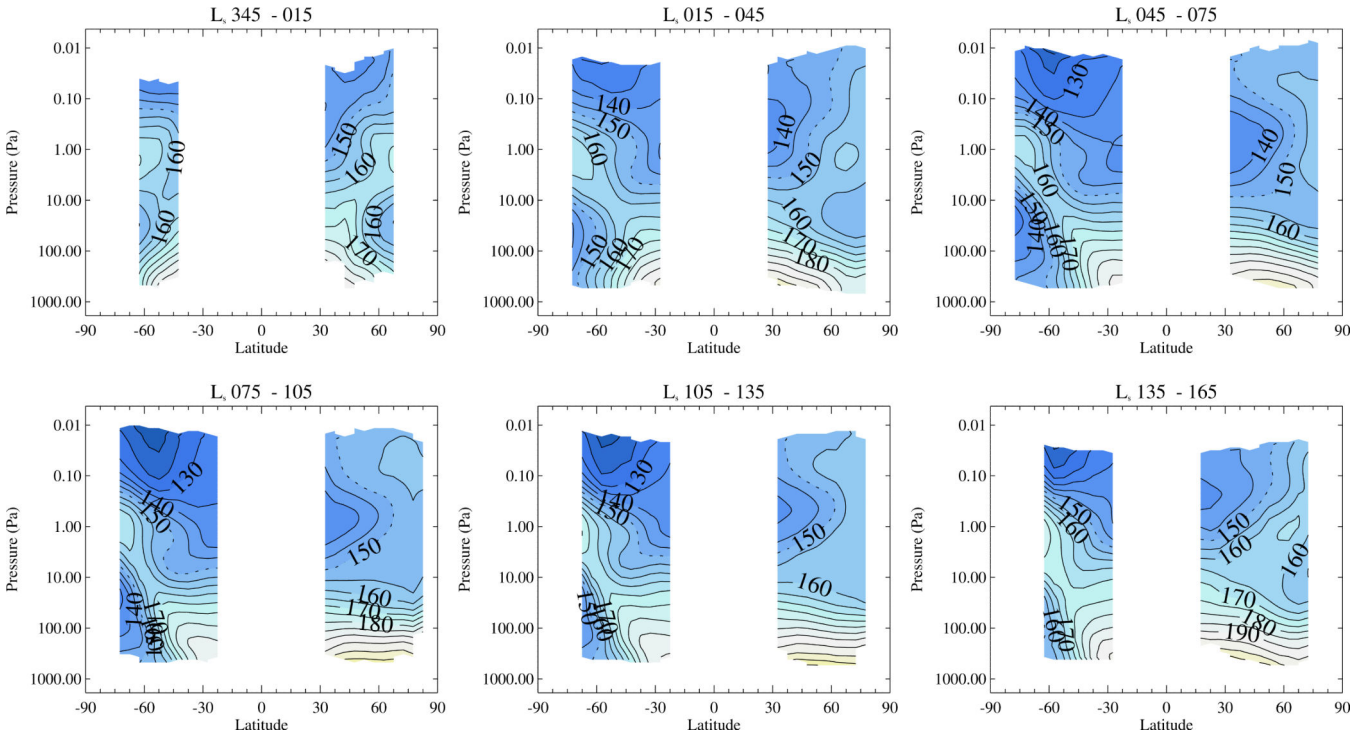

Figure 4.

$T_{\text{avg}}(m = 0)$ for the first six months of the Martian Year (Northern spring and summer). Calculated from MCS retrievals. The contour interval is 5K.

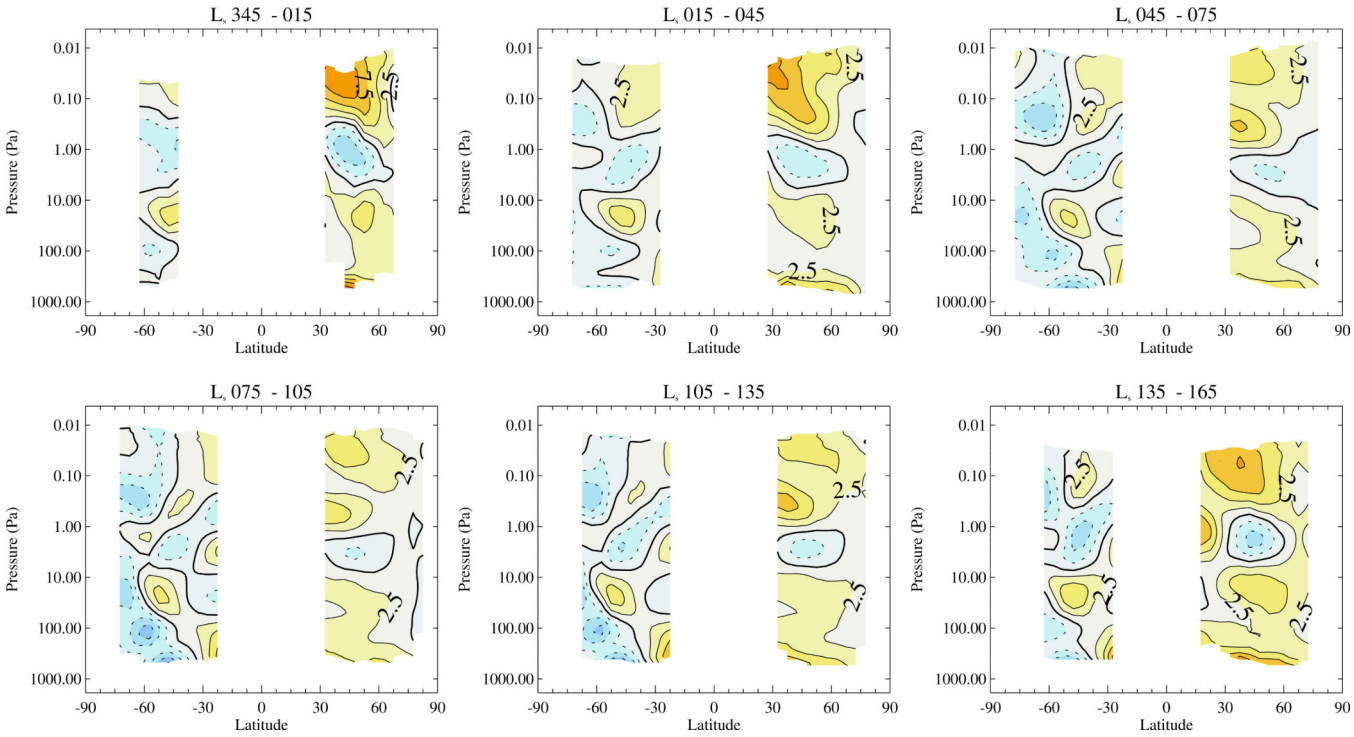

Figure 5.

$T_{\mathrm{diff}}(m = 0)$ for the first six months of the Martian Year (Northern spring and summer). Calculated from MCS retrievals. The contour interval is 2.5K.

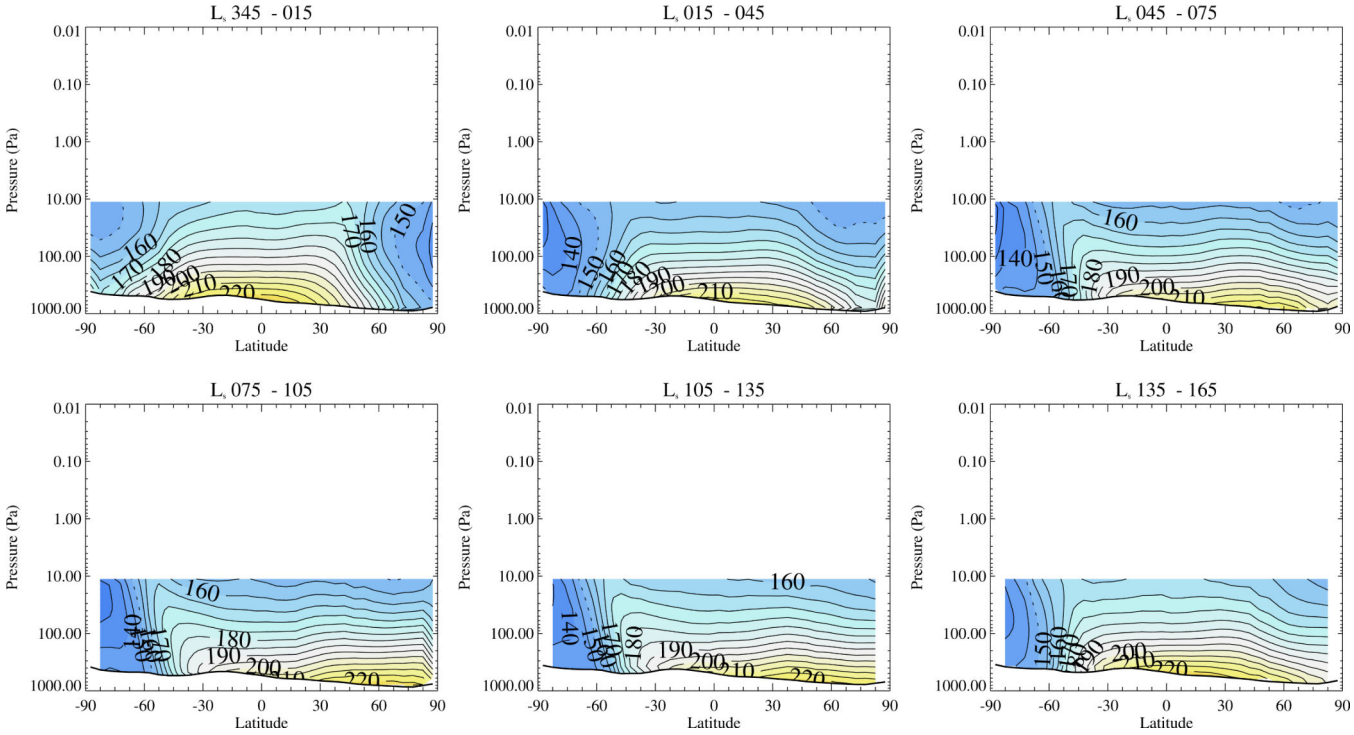

Figure 6.

Longitudinal mean of T_{avg} plotted from TES retrievals. Data is first binned into 64 longitude bins and 36 latitude bins, using the same vertical layers as the retrievals (21 layers), and binned here into 30° of L_s centered on 0°,30°,60°,90° etc. Contour interval is 5K. The dashed temperature contour is 150K (provided for reference).

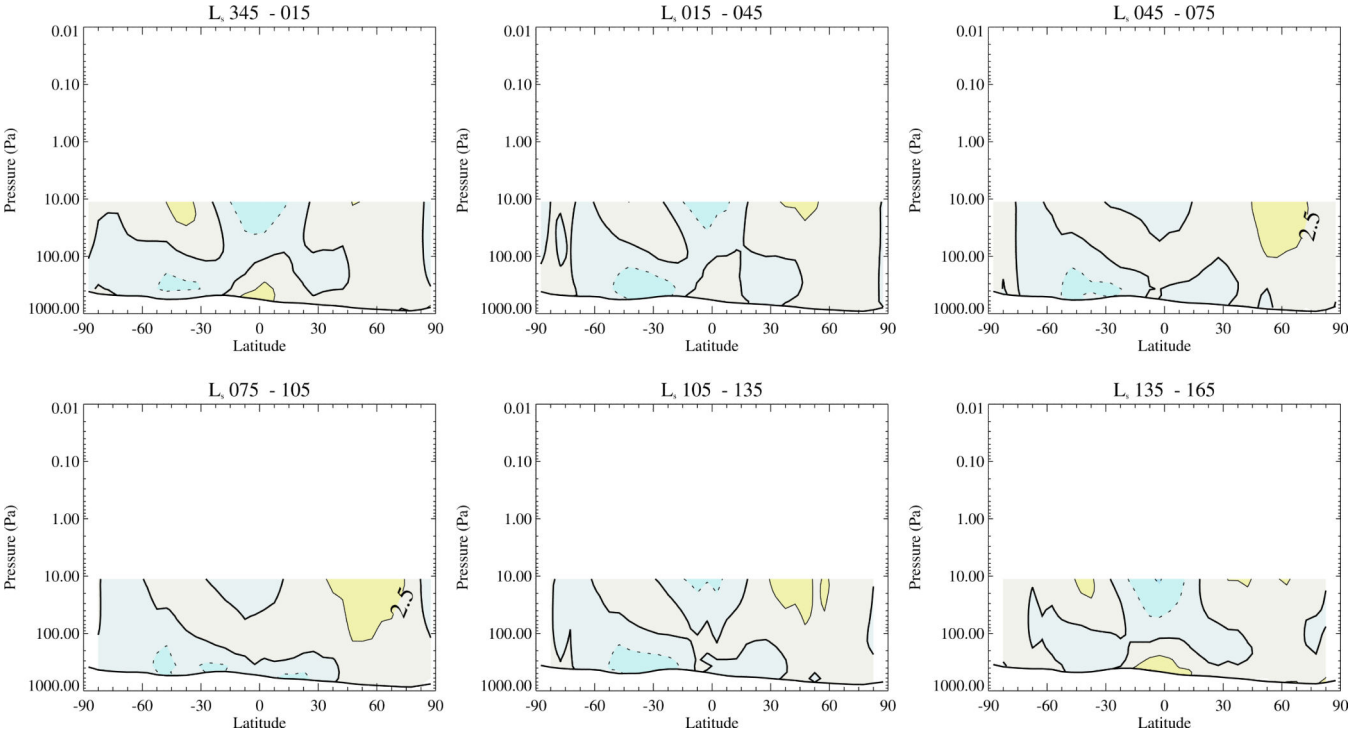

Figure 7.

As figure 6 using TES retrievals, but T_{diff} from equation 3. Contour interval is 2.5K. The thick temperature contour is 0K (for reference).

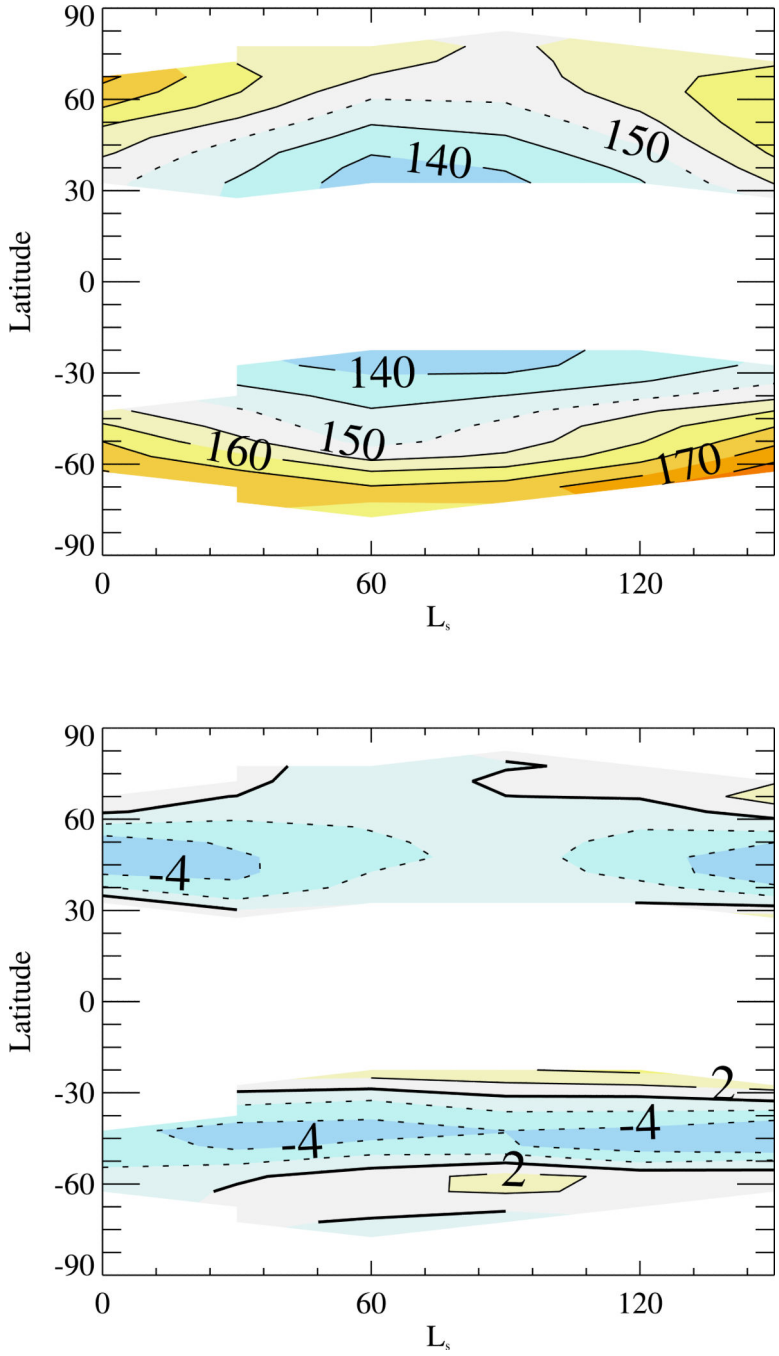

Figure 8.

(top) $T_{avg}(m = 0)$ and (bottom) $T_{diff}(m = 0)$ on the 2 Pa pressure level, from MCS data. Contour interval is (top) 5K and (bottom) 2K.

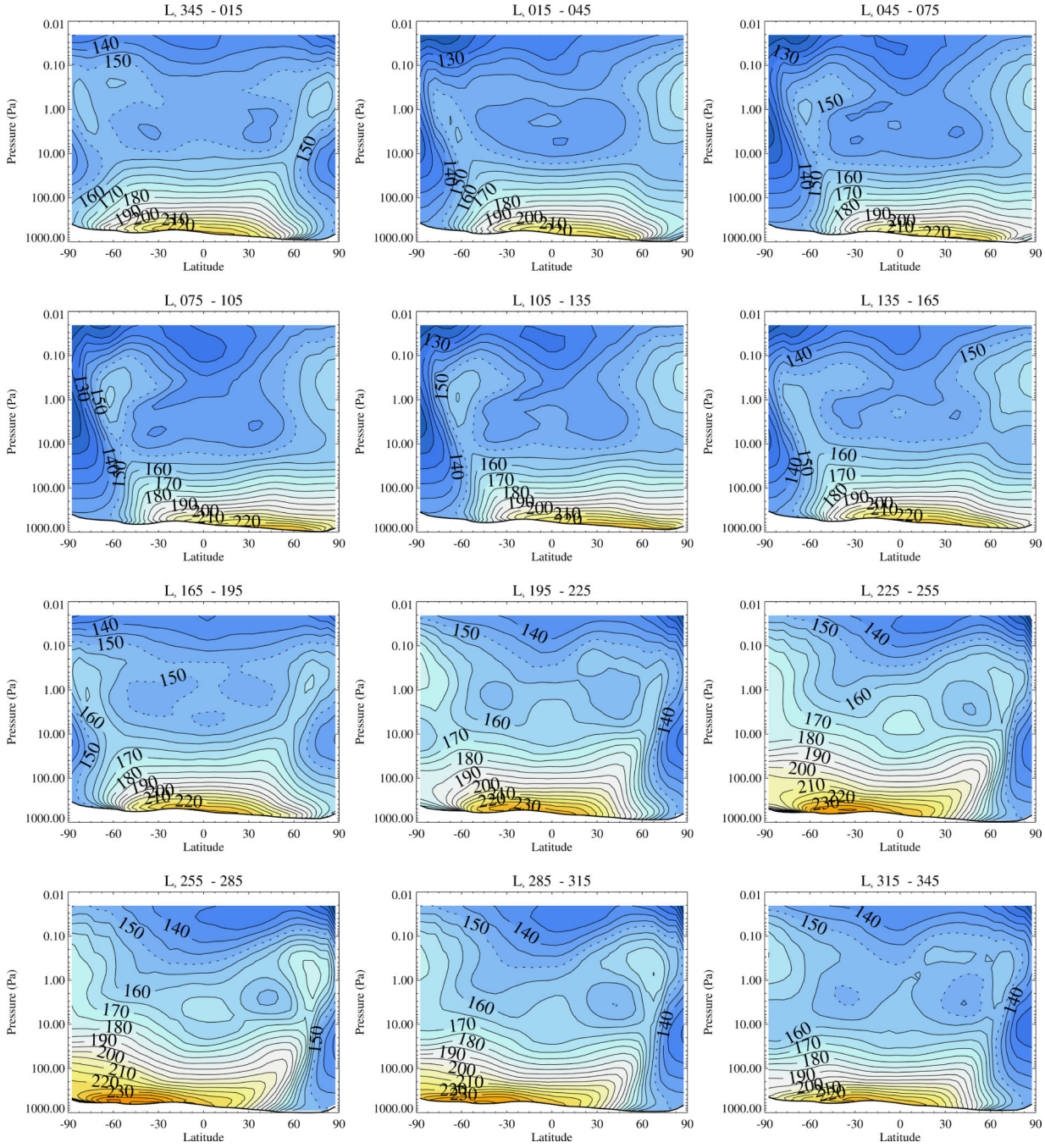

Figure 9.

As figure 2, but using data from an equilibrated WRF simulation for an entire Martian year. The data shown here was sampled every 3 hours (8 times daily) over 64 longitude and 36 latitude points, with 41 pressure layers. Contour interval is 5K and the contour colors are the same as in figure 2. The first two rows cover the same seasons as figure 2, the latter two rows are provided as a prediction of the as-yet unretrieved observations from MCS.

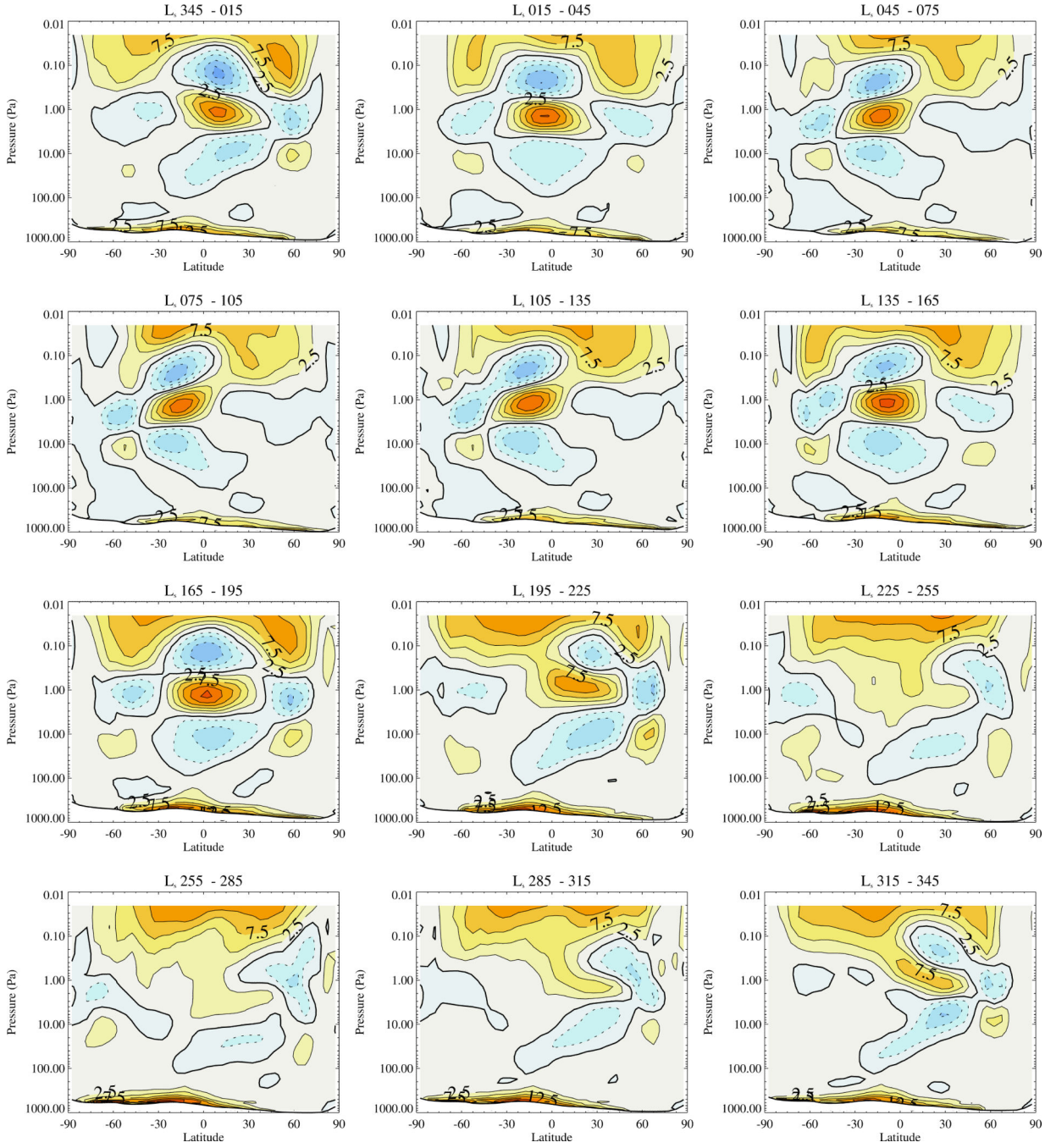

Figure 10.

As figure 3, but from WRF data for an entire Martian year. The data is described in the text and in the caption of figure 9.

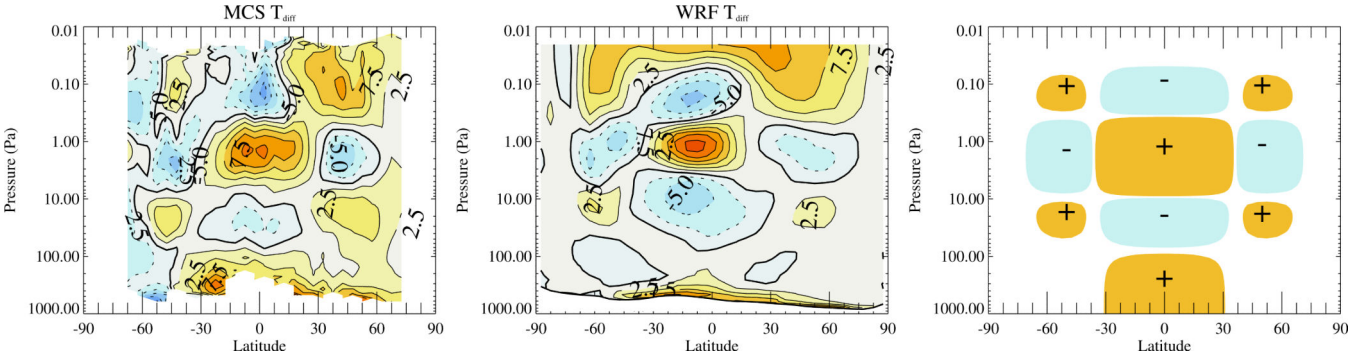

Figure 11.

T_{diff} between L_s135° and L_s165°, for MCS(left), WRF(center) and a schematic (right), contour interval is 2.5K .

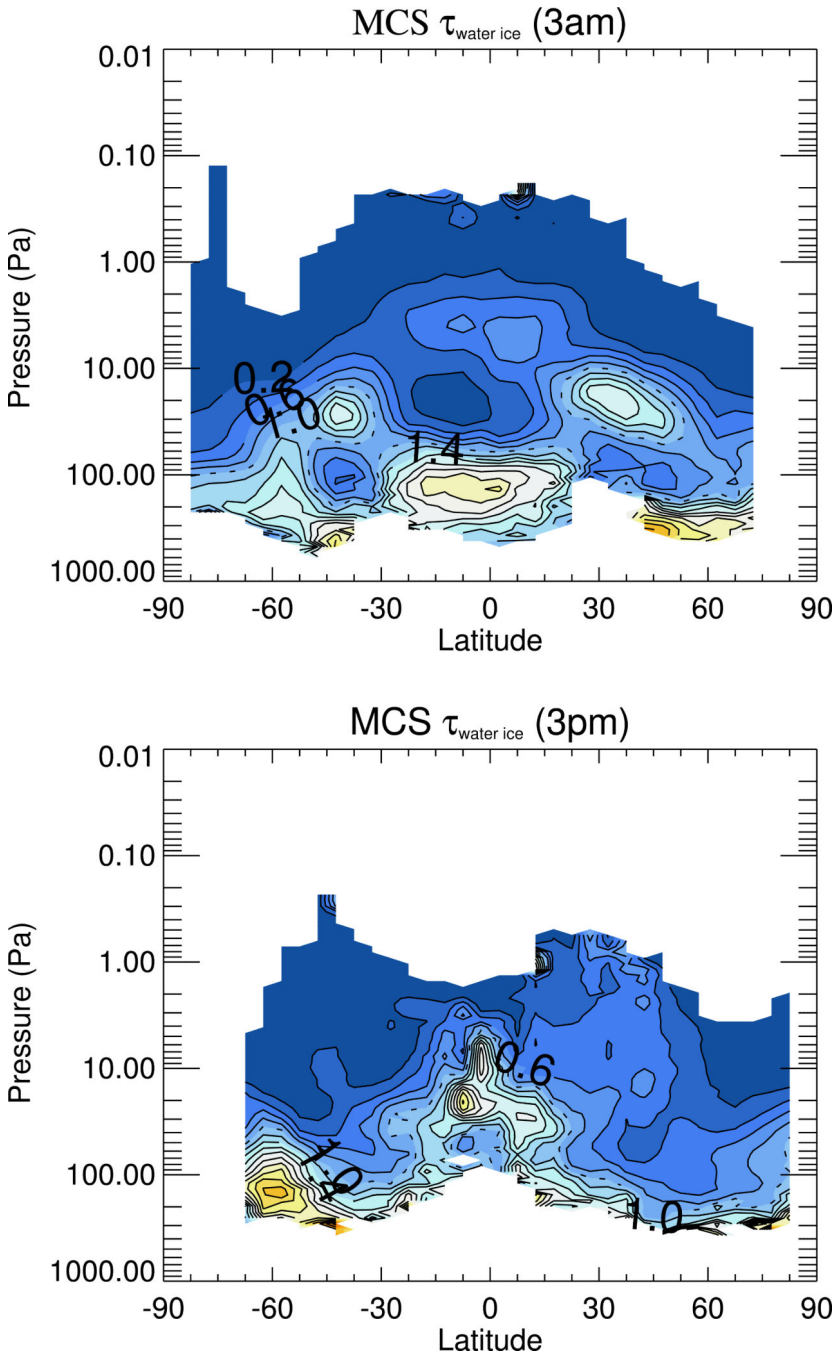

Figure 12.

Water ice opacity at 843cm^{-1} from the MCS retrievals at 3am (top) and 3pm (bottom) for the same data as figure 11, contour interval is 1×10^{-3}km^{-1}.

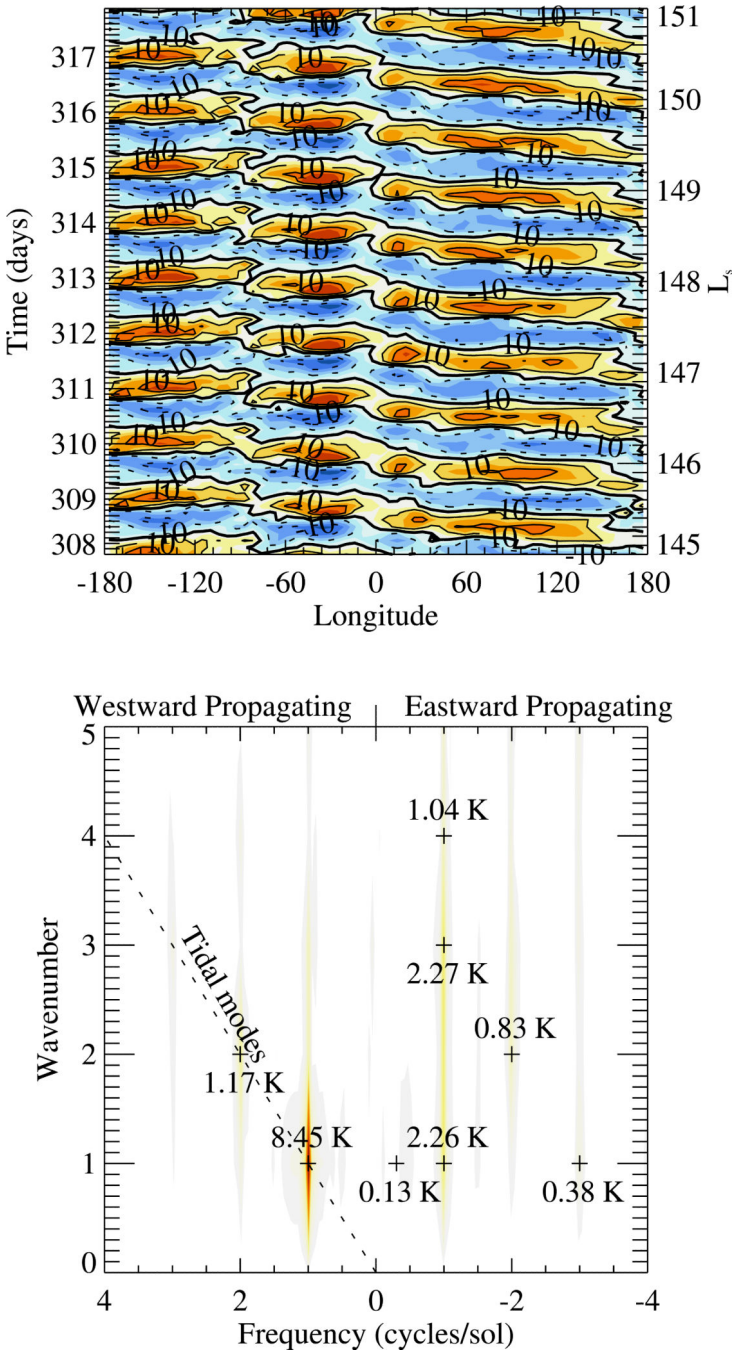

Figure 13.

(left) A sample of temperature data from the WRF simulation. Data here is sampled ever 3 hours (8 times daily) for 64 longitude points, for 15 S latitude and at 2 Pa, the time and zonal mean value has been removed. (right) The Fourier transform of this data, showing the tidal modes (along the diagonal dashed line), the Baroclinic modes (low frequency westerly waves) and a number of westerly propagating 1 cycle/sol waves.

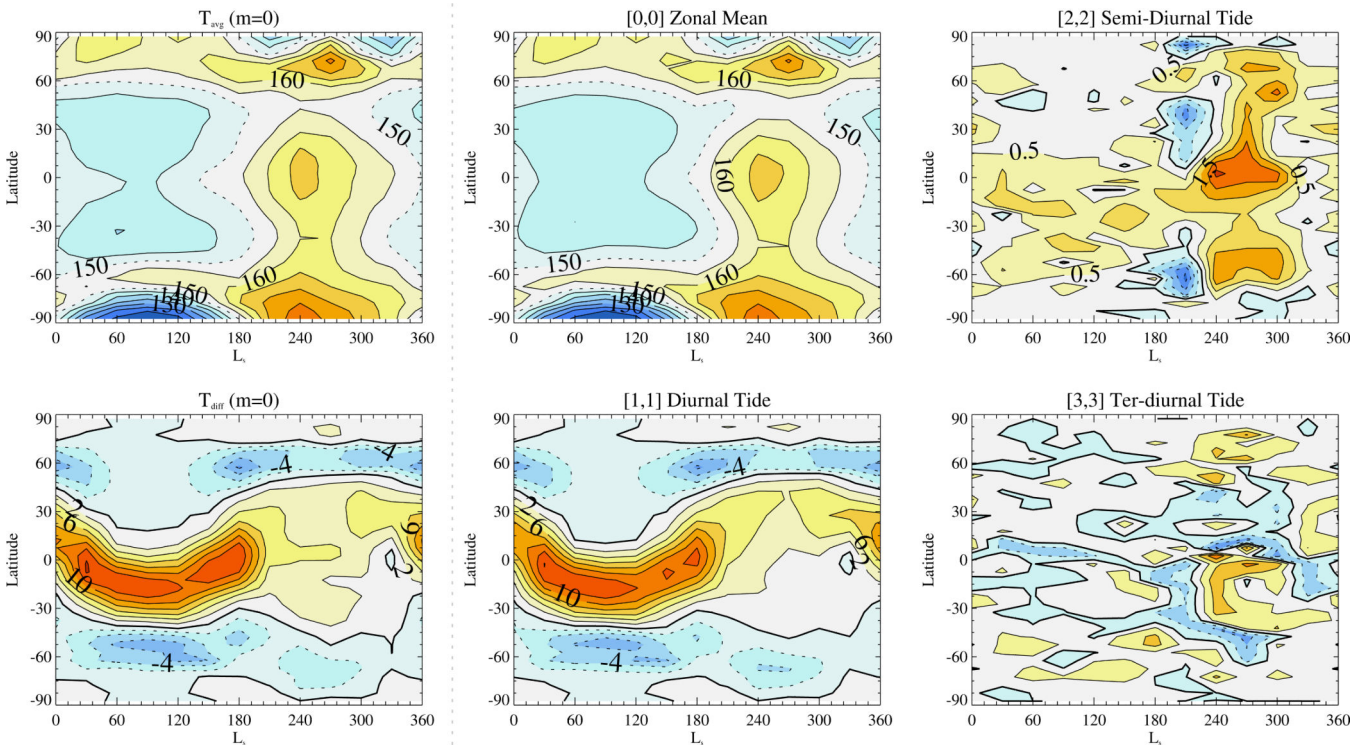

Figure 14.

M=0 local time wavenumber: (top row, left to right) T_{avg} calculated from the 3pm and 3am values, zonal and time mean magnitude calculated by Fourier Transform (FFT) of the full field, sun-synchronous semi-diurnal tide amplitude calculated by FFT. Contour intervals are 5K, 5K, 0.5K. (bottom row, left to right) T_{diff} calculated from the 3pm and 3am values, sun–synchronous diurnal tide magnitude calculated by FFT, sun–synchronous ter-diurnal tide magnitude calculated by FFT. Contour intervals are 2K, 2K, 0.25K. All of the data are from the simulation, taken on the 2Pa layer.

Table 1

Selected list of wave modes that contribute to each local time wavenumber *m*. Each pair of numbers refers to the wave parameters, listed as [s,σ]. SS means “sun–synchronous” here.

Figure	Local Time wavenumber	T_{avg} contribution	T_{diff} contribution
14	0	[0,0] Zonal Mean [2,2] SS Semi–diurnal tide	[1,1] SS Diurnal tide [3,3] SS Ter–diurnal tide
	1	[1,0] Stationary wavenumber 1 [1,2],[3,2]	[0,1] Symmetric mode [2,1]
	2	[2,0] Stationary wavenumber 2	[1,-1] Westerly DK1 mode [3,1]
	3	[3,0] Stationary wavenumber 3 [1,-2] Symmetric half-day wave	[2,-1] Westerly DK2 mode [4,1]